ORNL/SPR-2020/1729

Fracture Strength Determination Methods for Ceramic Materials Applied to Uranium Dioxide

Nuclear Technology Research and Development

Prepared for
US Department of Energy
Advanced Fuels Campaign

A. Nelson, C. Silva, A. Lupercio,
E. Moshkelgosha, R. Winters,
C. Doyle, M. Mamivand, S. Dillon,
B. Heuser, and B. Jaques
Oak Ridge National Laboratory

September 18, 2020
M3FT-20OR020201073

SUMMARY

The Advanced Fuels Campaign is currently focusing on development of accident-tolerant fuels that possess a range of property modifications intended to improve fuel performance during accident and transient conditions as well as extend license limits to burnups beyond 62 MWd/kgU. Both of these drivers have identified understanding and mitigating fuel cracking as a key performance criterion. Small-scale cantilever beam testing has been identified as a plausible method by which to collect fracture data for UO_2 as a function of chemical and structural evolutions introduced either during fabrication or irradiation. While this method has been found to be capable of providing data that are in reasonable agreement with literature for unirradiated UO_2, the inherently small sample volumes that can be sampled limit its ability to capture the statistical nature of mechanisms that govern the fracture of brittle ceramics. A biaxial flexure strength test was developed to be used for unirradiated UO_2. This method is standard in the community, but no systems presently in use at national laboratories, universities, or private companies are available to be used for nuclear fuel materials. This report describes the operation and benchmarking of this system, which has been validated for a number of common oxides. Future work will extend this system to characterization of both doped UO_2 and other relevant microstructural modifications that can also be measured using small-scale cantilever beam testing. Comparison of datasets collected using both methods will allow the overall applicability of small-scale techniques to be assessed and provide confidence or bounds on their use for irradiated fuels.

This page is intentionally left blank.

CONTENTS

This page is intentionally left blank.

FIGURES

TABLES

This page is intentionally left blank.

ACRONYMS

AFC	Advanced Fuels Campaign
ASTM	American Society for Testing of Materials
ATF	Accident-tolerant fuel
BSE	Backscatter electron
EDS	Energy-dispersion spectroscopy
FE	Finite element
FIB	focused ion beam
ICP-MS	Inductively coupled plasma–mass spectrometry
LWR	light water reactor
MRF	Materials Research Furnaces, Inc.
MSZ	Magnesia-stabilized ziconia
MTS	Materials Test System
NIST	National Institute of Standards and Technology
ORNL	Oak Ridge National Laboratory
PCI	pellet-cladding interaction
SEM	scanning electron microscopy/microscope
TRS	Transverse rupture strength
UO_2	uranium dioxide
XRD	X-ray diffraction
YSZ	Yttria-stabilized zirconia

This page is intentionally left blank.

FRACTURE STRENGTH DETERMINATION METHODS FOR CERAMIC MATERIALS APPLIED TO URANIUM DIOXIDE

1. INTRODUCTION

Uranium dioxide (UO_2) fuel is used as fuel in light water reactors (LWRs). While the fuel pellet is technically the first engineering barrier for radionuclide release, pellet fracturing at intermediate- to high-burnup values releases fission gases into the fuel rod plenum [1, 2]. Therefore, the true engineering barrier is the fuel cladding, which performs very well in LWR environments [3]. The extreme temperature gradients generated by fission energy and the low thermal conductivity of UO_2 quickly induce radial cracking in UO_2 during operation [4]. Cracks in the fuel provide opportunities for fuel relocation, increased fission gas release, and pellet-cladding mechanical interaction (PCMI) [5]. The ability to predict and engineer the fracture of UO_2 fuel pellets using modern computational tools is therefore a key engineering goal that has been the focus of ongoing experimental and computational efforts [6, 7]. Accurate predictions of fuel pellet cracking during operation requires knowledge of more complex phenomena, but improved understanding of the fundamental fracture behavior of unirradiated UO_2 is first necessary.

The Advanced Fuels Campaign (AFC) is currently focusing on development of accident-tolerant fuels (ATF) that possess a range of property modifications intended to improve fuel performance during accident and transient conditions. In addition, efforts are under way to understand the phenomena that limit performance at high burnups in an effort to extend license limits to burnups beyond 62 MWd/kgU. Both of these drivers have identified understanding and mitigating fuel cracking as a key criterion. A previous AFC report provided an overview of the current mechanical property database for UO_2 and evaluated the potential for small-scale test methods to address the challenge that reference materials face for examination of irradiated fuel systems [8]. This work found that data collected for pure UO_2 collected using cantilever beam testing was in reasonable agreement with that found in the literature and would provide a plausible means to measure the evolution of fracture behavior of grain boundaries or other features following irradiation.

However, the major limitation of small-scale cantilever beam testing is that it cannot capture the true statistical nature of fracture in ceramics. Fracture and failure of brittle materials is a stochastic process. This has historically required testing of high numbers of samples in order to achieve statistical confidence, typically expressed as a Weibull modulus. This report extends the use of microcantilever beam testing to more fully assess systems of relevance to ATF development, specifically the impact of Cr dopants on fracture toughness. In parallel, development has begun on the deployment of biaxial flexure strength testing for uranium fuels. Biaxial flexure strength testing is a conventional method for fracture determination and provides transverse rupture strength (TRS) and Weibull statistics for brittle materials according to accepted standard testing methods. This report describes progress made in FY 2020 in this area and summarizes future research needs.

2. THEORY AND BACKGROUND

The mechanical properties of UO_2 have been analyzed to a limited extent since the early years of the nuclear era, but the challenges of both the material and characterization of irradiated fuels have greatly limited the experimental database [8]. Previous research has demonstrated the applicability of small-scale microcantilever beam testing to measurement of fracture in pure UO_2 [9]. However, traditional methods will also be necessary to better characterize fracture in unirradiated UO_2 and controlled variants to provide confidence in testing performed using small-scale methods. The development of a biaxial flexure test as well as use of small-scale microcantilever beam testing is described here.

2.1 Biaxial Flexure Test

Due to the brittle nature of ceramics, their mechanical properties are rarely measured using typical tensile tests employed for metals. Historically, the flexural strength or TRS of ceramics has been commonly determined using 3- and 4-point bend tests using 3×4×45 mm rectangular bend bars per ASTM standard C1161-13. However, a comprehensive statistical analysis of flexural test data using bend bar techniques is limited due to difficulties in producing samples with the required geometries and dimensions. In addition, extraneous flaws introduced along the edges during the fabrication of the bend bars often become the origin of fracture [10]. In contrast, the biaxial flexural strength test requires a simple right cylindrical test specimen. Additionally, 3- and 4-point bend tests only provide information about the mechanical properties of ceramic materials under uniaxial loading [10]. It is important to use other methods to evaluate the mechanical properties under multiaxial loading states to obtain a more accurate rupture strength, particularly for specimens loaded in non-uniaxial states during service.

Common biaxial flexural strength tests include ring-on-ring, piston-on-3-balls, or the ball-on-ring, all of which work to reduce friction during testing [11]. Several studies [11–13] have used Equation (1) to calculate the transverse stress (σ) and obtain the TRS of similar ceramics:

$$\sigma = \frac{A * F}{t^2}, \tag{1}$$

where t is the specimen thickness, F is the applied force, and A is a dimensionless factor that depends on the geometry of the specimen and loading ball, the ring diameter, and the Poisson's ratio of the loading ball and test materials. The factor A is calculated using Equation (2) for a multiple ball or ball-on-ring test:

$$A = \frac{3}{4 * \pi}\left[\left(2(1 + \nu_S) * ln\frac{a}{b}\right) + \frac{(1 - \nu_S)(2a^2 - b^2)}{2R^2} + (1 + \nu_S)\right],$$

(2)

where ν_S is the Poisson's ratio of the test material, a is the radius of the support ring, R is the radius of the test specimen, and b is the contact radius of the loading ball. The contact radius of the loading ball b can be calculated using an equivalent radius, $\overline{b} = \sqrt{1.6b^2 + t^2} - 0.675t$, which can be reduced to $\overline{b} = \frac{t}{3}$.

2.2 Weibull Statistics Theory

The fracture of brittle materials, such as ceramics, do not follow the same trend as metallic materials. Instead, cracks typically initiate from flaws in the material, and the strength of the material is dependent on the size of the largest critical flaw in each specimen [13]. The statistical behavior of brittle materials indicates that the probability of failure increases with increasing load and with larger sample volumes [14]. The fracture analysis of these types of materials requires understanding the behavior of many cracks, which are assumed to be stochastically distributed in the material. The flexural strength of a brittle ceramic material cannot be described using a single stress value. Hence, a probability function must be used to quantify the characteristic strength, probability of failure or reliability, and flaw population and distribution of brittle materials. One common method of analyzing the statistical fracture of ceramics is the Weibull distribution of the probability of failure. Describing fracture behavior using Weibull statistics assumes that (1) the structure must fail if one single flaw becomes critical and (2) large flaws do not interact [14].

Fracture analysis with the above assumptions allows us to use a cumulative probability of fracture defined as $F_S(\sigma) = 1 - \exp(-N_C,_S(\sigma))$, where $N_C,_S(\sigma)$ is the mean number of critical cracks in a specimen with size and shape S and a homogeneous crack size frequency is present. Integrating $N_C,_S(\sigma)$ over volume, the classical relationship for the probability of failure (P_f) using Weibull statistics is derived:

$$P_f = F(\sigma,V) = 1 - \exp\left[-\frac{V}{V_0}\left(\frac{\sigma_f}{\sigma_0}\right)^m\right], \tag{3}$$

where σ_f is the fracture strength, σ_0 is the characteristic strength, m is the Weibull modulus, V is the specimen volume, and V_0 is the starting specimen volume [5]. Assuming the effective volume does not significantly change during the biaxial flexural test, the equation can be rearranged into

$$\ln\ln\left(\frac{1}{1-P_f}\right) = m * ln\left[\frac{\sigma_f}{\sigma_0}\right] . \tag{4}$$

The Weibull parameters σ_0 and m can then be determined by plotting the equation in the form of a line, $y = m * x + b$ [15]. The characteristic strength is defined as the stress value at which 63.2% of all samples fail, and the Weibull modulus provides information about fracture data scatter of the samples [16]. The larger the Weibull modulus the less variation in fracture stress and the higher the degree of homogeneity between samples.

2.3 Fracture Strength of UO_2

Fracture of ceramic materials creates an impediment to measurement and modeling. Fracture behavior is typically defined in terms of a stress intensity factor, K_I defined as $\sigma\gamma\sqrt{c}$, where σ is the applied stress, γ is a dimensionless parameter that depends on the crack and loading geometries, and *c* is the flaw size. Mode 1 fracture is the most important for the behavior of fuel pellets during operation, as thermal gradients induce tensile "opening" behaviors that lead to crack propagation. For Mode 1, K_{IC} is the critical stress intensity factor, or *fracture toughness*. Material will fracture if $K_I > K_{IC}$.

It is less familiar and more complex to measure the fracture behavior of ceramics. While K_{IC} is the most relevant fundamental parameter, it is also the most challenging to directly access experimentally. Instead, the *modulus of rupture* (σ_r)— the maximum tensile stress in the surface of the beam at fracture—is measured using either a 3- or 4-point bend test. Modulus of rupture is also referred to as *flexural strength*, *fracture strength*, and *bend strength*. The geometry of a 3- or 4-point bend test is coupled with the introduction of a known flaw geometry, which is introduced through a notch, to determine the fracture toughness, K_{IC}, of the material.

The challenges of the test methodologies outlined above when applied to nuclear fuels, even in the unirradiated condition, are apparent from the description. Foremost, a 3- or 4-point bend test that is performed to determine the modulus of rupture is influenced by sample-dependent variations in the density and distribution of microscopic flaws and the possible crack initiation sites in the material. A high number of tests is needed to ensure statistical relevance. The use of notched samples mitigates this challenge to some extent, but it requires notching, and it also provides a measure of the fracture's toughness rather than a modulus of rupture. Fracture toughness is a more valid theoretical measure of the resistance of a material to brittle failure, but mechanistic fuel performance codes are more equipped to consider failure in terms of the modulus of rupture [6]. An additional challenge occurs with the sample geometries needed for bend testing. A typical bend bar that is used for either 3- or 4-point bending requires a long, thin bar measuring 3 × 4 × 50 mm, for example. This shape is not amenable to powder processing, which is the process used to fabricate UO_2 fuel pellets. However, development of methods capable of fabricating bar geometries is warranted as it would facilitate benchmarking of proposed alternative methods for determination of fracture behavior in ceramic nuclear fuels.

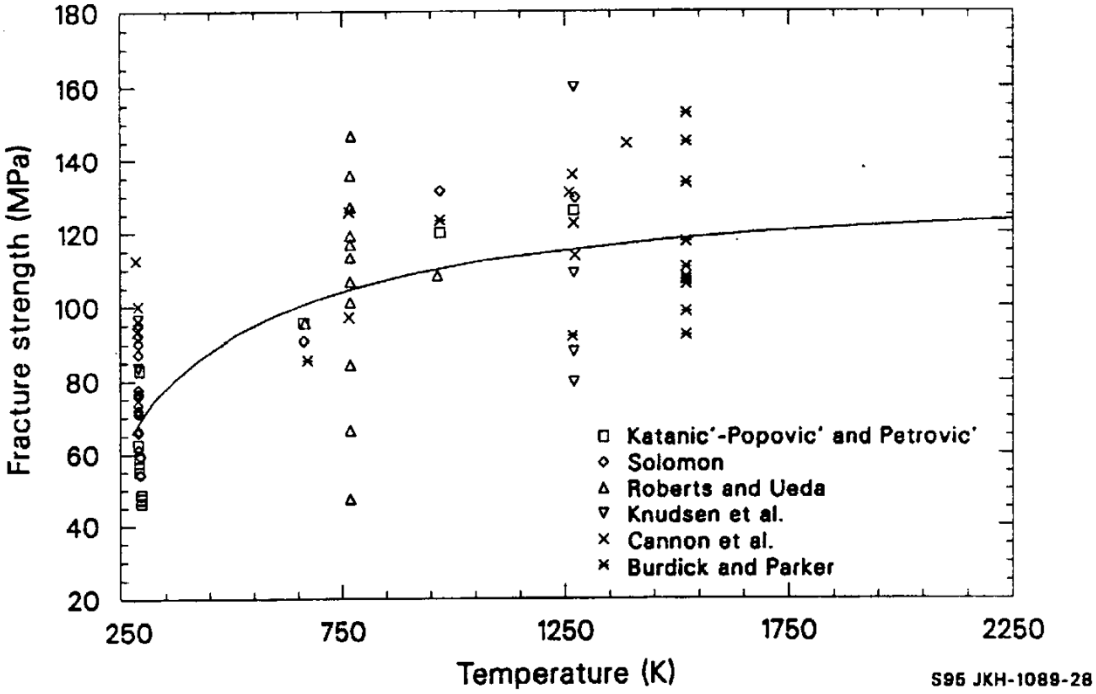

Figure 1. Fracture strength (modulus of rupture) of unirradiated, stoichiometric UO_2 as a function of temperature as reported in the MATPRO database [14].

The data plotted in Figure 1 highlight the typical scatter of modulus-of-rupture measurements. Even at room temperature, values range from 45 to 115 MPa. This result is expected given the unavoidable distribution of flaw sizes and orientations in a ceramic material. This reality has driven ceramic engineers to incorporate the use of Weibull statistics to capture the probability of failure for a ceramic component subjected to tensile stress. This approach has been explored numerically for UO_2 fuels [13], but no experimental data have yet been generated to facilitate a rigorous analysis.

3. SAMPLE FABRICATION

As mentioned in the introduction, AFC is exploring a range of LWR fuel concepts under the core campaign and through collaborative industry activities. Although a range of options including particle fuels and high-density systems have been evaluated under the ATF program, so-called "evolutionary" approaches using minor modifications to UO_2 are currently being prioritized given their near-term applicability. For the present work, two approaches were taken. First, pure UO_2 and Cr-doped UO_2 were fabricated at Oak Ridge National Laboratory (ORNL) using reference processes. These samples were then characterized using small-scale cantilever fracture test methods. Second, surrogate oxide samples were fabricated of geometries necessary for biaxial flexural strength testing. Surrogates were used at this point to demonstrate and benchmark the technique before proceeding to testing of UO_2, given the cost and quantities of material needed for this method. The fabrication and characterization of all materials are described below.

3.1 Surrogate Sample Fabrication and Characterization

3.1.1 Fabrication of Yttria-Stabilized Zirconia and Magnesia-Stabilized Zirconia

Commercially purchased ceramic benchmark materials of 99.8% pure alumina, 3.5mol% Y_2O_3-partially stabilized zirconia (YSZ), and 3mol% MgO-partially stabilized zirconia (MSZ) were purchased in the form of right cylindrical rods with a diameter of 15.9 mm. From these rods, test specimens were cut close to 1.5 mm in height using a low-speed saw with a low-concentration diamond blade and a propylene glycol cutting fluid. The pellets were ground down to approximately 1.5 mm in height using an UltraPrep 45 µm diamond disc (Buehler) and then fine-tuned with parallel faces within ±0.02 mm using 180 grit silicon carbide paper. Figure 2 provides photographs of the prepared samples. This method allowed for greater control of the sample preparation as the diamond discs ground through the material at a faster rate than the 180 grit silicon carbide paper. Sample height was measured using a micrometer with five perimeter and three center measurements, which were averaged to produce the height value used in the TRS calculations.

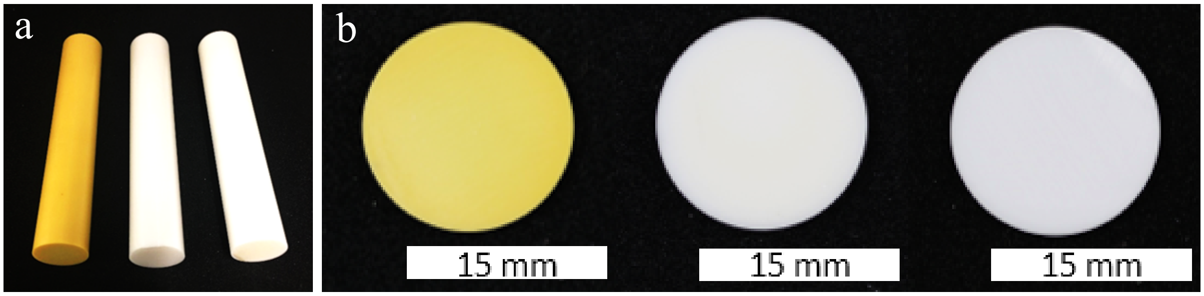

Figure 2. Benchmark rods (a) and pellets (b) in order from left to right are MSZ, alumina, and YSZ as prepared for biaxial flexural strength tests.

3.1.2 Characterization of Alumina, Yttria-Stabilized Zirconia and Magnesia-Stabilized Zirconia

The structure and phase purity of alumina,YSZ, and MSZ samples were characterized prior to benchmarking the biaxial flexure strength. Accordingly, no unexpected phases or behaviors were observed here, which was verified using x-ray diffraction (XRD) ((results not included in this report). Scanning electron microscopy (SEM) was used to obtain images of the alumina, MSZ, and YSZ microstructure to measure the average grain size, as seen in Figure 3. Archimedes and geometric density measurements for alumina, MSZ, and YSZ were recorded in Table . Grain size measurements were performed on thermally etched samples using ASTM standard E112-13 for alumina and ASTM standard E112-12 for MSZ and YSZ; grain size measurements are also recorded in Table .

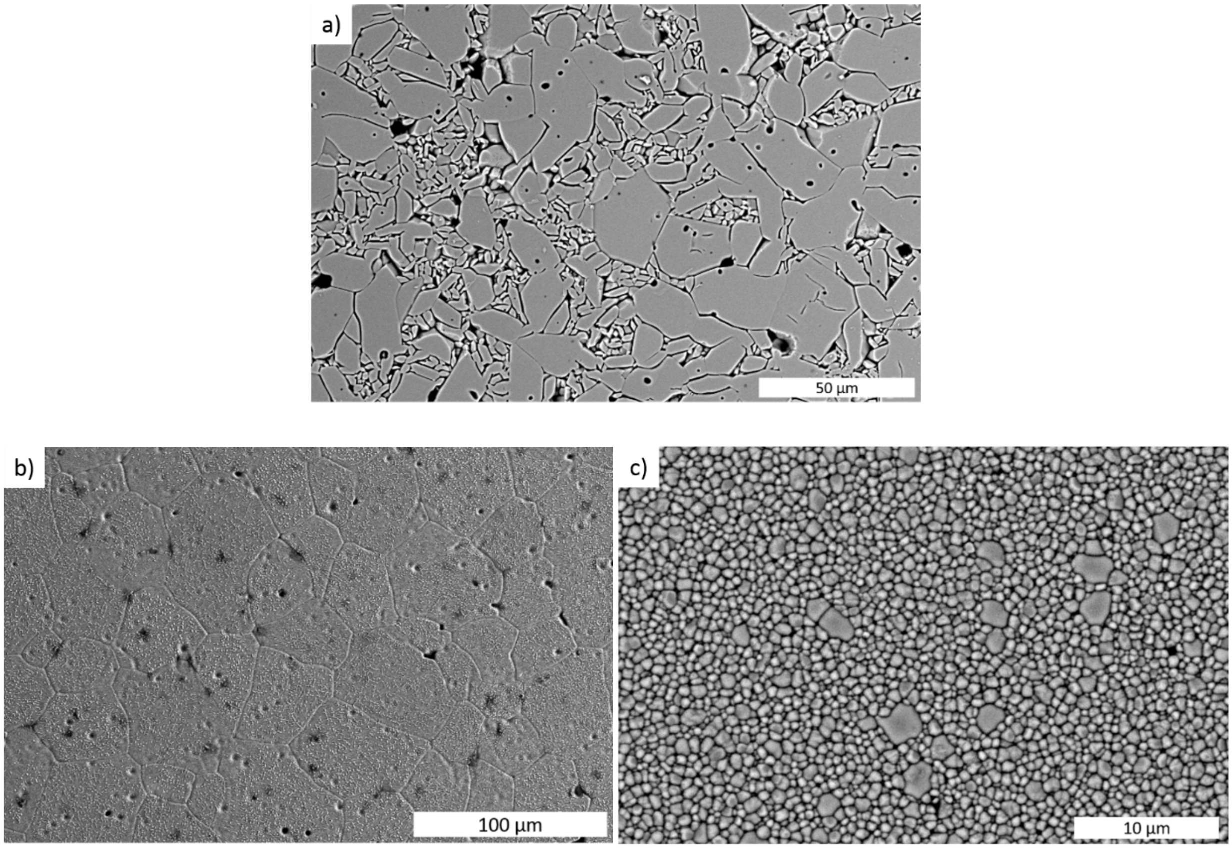

Figure 3. SEM micrographs of microstructure for thermally etched (a) alumina, (b) MSZ, and (c) YSZ test specimens. Specimens have a grain size of 5.6–63.5 µm (trimodal), 35 µm, and 0.7–1.9 µm (bimodal), respectively.

Table 1. Density and grain size measurements for alumina, MSZ, and YSZ.

Material	Density			Grain Size (µm)	Grain Size Mode
	Reference (g/cm^3)	Archimedes (±2% TD)	Geometric (±2%TD)		
Alumina	3.92(9)	99	97	5.6, 11.2, 63.5	trimodal
MSZ	5.79	99	97	35	unimodal
YSZ	6.10(16)	98	94	0.7, 1.9	bimodal

3.2 Fabrication of UO_2 and Cr-doped UO_2

3.2.1 Fabrication of Nominally Pure UO_2 and Doped UO_2

Uranium dioxide powder in its depleted form was purchased from Areva nuclear power company, USA. Inductively coupled plasma–mass spectrometry (ICP-MS)/ESPEC chemical analysis of this source material showed that there are impurity elements such as Al, Ca, Cr, Fe, Mg, Mn, Mo, Na, Si, V, and Zn at 10–25 ppm levels, along with some other minor elements at <1 ppm level. This as-received oxide powder consisted of two main chemical phases according to the XRD studies: UO_2 and U_3O_8 as depicted in the bottom XRD pattern in Figure 4. Full profile fitting of the XRD pattern also showed that U_3O_8 is present at up to 9 wt.%, with the remainder being $UO_{2\pm x}$. To avoid disintegration of UO_2 pellet samples, it is necessary to have the starting material in its stable dioxide (UO_2) form. Therefore, a part of the as-received material was calcined at 650°C for 5 h under a flowing Ar-4%H_2 reducing environment in an alumina crucible to make UO_2 (top figure in Figure 44), which was used as the UO_2 feedstock material for the pellet samples fabricated, as discussed below. As shown by the top XRD pattern in Figure 4, the calcined sample only consisted of UO_2.

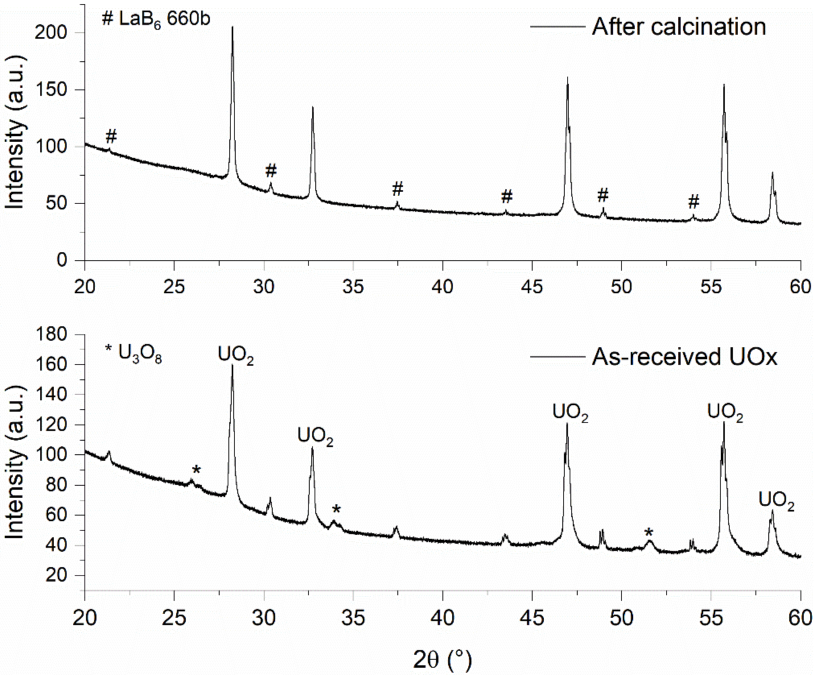

Figure 4. Powder XRD patterns of the as-received and calcined uranium oxides samples.

Two dopants were used in the samples discussed here: chromium (III) oxide, Cr_2O_3, was purchased from Alfa Aesar with a 99.97% (metal basis) purity, and aluminum (III) oxide (α-Al_2O_3) was purchased from Sumitomo Chemical Co., LTD. The particle sizes of the starting Cr_2O_3 and Al_2O_3 materials were 1–2 μm and 0.5 μm, respectively. Precursor powder samples were weighed using a Sartorius balance (120 g capacity and 0.0001 g readability). The balance has been calibrated yearly and validated daily using Troemner check weights (S.N.4000024311). A feedstock material was prepared using 10.2304 and 0.0106 g of UO_2 and Cr_2O_3, respectively, to obtain the 1000 wppm Cr_2O_3/UO_2 samples (actual Cr_2O_3 concentration is 1035 wppm). Sample batch sizes of 1–2 g were also used for different Cr_2O_3 concentrations (500–2000 wppm) in the as-fabricated or green pellets. These starting materials, including UO_2, together with a ½-in. ZrO_2 impactor sphere, were separately ball-milled for 10 min using a SPEX

Mixer/Mill 8000M in a dry condition, which could lead to a slight hyperstoichiometry of oxide samples due to potential oxidation. Further mixing was conducted using a Vortex-Genie 2 vortex mixer for 1 min. The addition of the dopants into the UO_2 was performed by first mixing the required dopant masses with UO_2 in a mortar and pestle and then mixing them with a SPEX mixer.

The milled UO_2-Cr_2O_3 and UO_2-Cr_2O_3-Al_2O_3 powders were loaded into a 10.3-mm internal diameter die and pressed into pellets using a 100–300 MPa pressure at room temperature. Pressures were varied in an attempt to explore whether this variable impacted the microstructure or density, but no correlation was found. Results are therefore presented here without specific consideration of pressing pressure. A 3% stearic acid solution was applied on the parts of the die as a releasing agent. Using a powder sample that was close to 1 g, a pellet in its unheated (green) form with a thickness of 2.0–2.2 mm was obtained. All the heat treatments of the pellet samples were carried out using a Materials Research Furnaces, Inc. (MRF) Mo/W metal well-furnace. The samples were heat treated at different temperatures ranging from 1,150–1,750°C, with varied holding times (6–48 h). In general, furnace ramping rates of 5 and 3°C/min were used from room temperature to 1500 and 1700°C, respectively. Furnace cooling was carried out using three different rates: 3°C/min for 1700 to 1500°C, 5°C/min for 1500 to 1000°C, and 10°C/min for 1000°C to room temperature. These furnace ramping and cooling rates were used to lower any chance of sudden temperature jumps that could shock the sample pellets causing them to break. All the heat treatments were also carried out under a flowing Ar-4%H_2 cover gas environment. The use of these experimental conditions will be discussed further in the results section.

Sintered sample weighing was performed using a Mettler Toledo analytical balance, which has been calibrated yearly. It was also validated to a ± 0.0001 g accuracy using check weights before and after its daily use. Pellet dimensions were determined using a calibrated Mitutoyo 500-196-30 digital caliper. Densities of the green pellets were determined using pellet weights and geometrical dimensions using the $\frac{m_s}{\pi \times r^2 \times h}$ formula, where pellet mass, radius, and height are represented by ms, r, and h, respectively. Archimedes principle was used to determine the sintered pellet densities with a Mettler Toledo density kit MS-DNY-54: $\rho_s = \frac{m_s}{(m_s - m_l)} \times \rho_l$, where ρ_s, ρ_l, m_s, and m_l are density of the sample, density of the liquid (deionized water) medium, (dry) mass of the sample, and sample mass in the liquid, respectively.

3.2.2 Characterization of Nominally Pure UO_2 and Doped UO_2

Two cut pieces of the sample representing the axial direction and along the normal direction of the pellet were mounted in conductive (graphite) epoxy mounts for microstructural evaluation. A benchtop Phenom XL (Nanoscience Instruments) SEM equipped with an energy dispersion spectroscopy (EDS) system was used to observe the microstructure of the samples and to qualitatively analyze the samples' constituent elements. SEM micrographs were collected using secondary electron (SE) and backscattered electron (BSE) modes with a 10–15 kV voltage range. SEM micrographs of axial and normal samples were collected using at least three different random areas representing grain morphology of the samples at same or different resolutions. An area consisting of more than 100 grains was selected at the lowest resolution in the first step of the grain size determination. Areas with more than 50 grains in the high-resolution micrographs were selected for further grain size determination. The size or the length of each grain was determined manually using the longest grain direction. Because samples cut in two directions (axial and normal to the sample surface) were imaged, the average grain size of the samples was determined using the sizes of ~500 grains, allowing for better precision. Standard deviation is also presented, along with the average grain size as determined for each sample.

XRD patterns of the powder samples were collected using a Bruker D2 Phaser x-ray diffractometer equipped with Cu k_α radiation. Full-profile fitting of the XRD patterns was performed using General Structure Analysis System software in which the lattice parameter of UO_2 phase was refined using Rietveld refinement. A modified Scherrer equation and the Williamson-Hall plots were used to determine the samples' lattice strains, which were not significant and not reported here as a result of the deviation of data from the expected linear variation of the Williamson-Hall plots. Crystallite sizes were also determined using the individual peak based on the modified Scherrer equation. In this XRD study, instrumental corrections were performed using the lanthanum hexaboride (LaB6)-660b National Institute of Standards and Technology standard. Chemical analysis of a few selected post-sintered samples was performed using ICP-MS by MCLinc (Materials and Chemistry Laboratory, Inc). A sample size of ~0.01 g was used for the analysis for each sample.

Undoped UO_2 pellets were made using the calcined UO_2 starting material in the powder form. These samples were sintered at 1,700°C under Ar-4%H_2 for 6 and 10 h holding times. The UO_2 pellet sintered for 6 h had a 5.90 g/cm^3 (53.7% TD) density in its green state and a 10.52 g/cm^3 (95.9% TD) density after its sintering. The average grain size of the sample sintered for 6 h was 8 ± 5 µm, where ± 5 µm is one standard deviation (σ) of the mean value of 8 µm. The density of the pellet sintered for 10 h was 10.5 g/cm^3 (95.4% TD). Figure 5(a) shows an example of the microstructure of this sintered, undoped UO_2 sample. While an average grain size of 12 ± 6 µm was determined for the sample, ~90 and 10% of grains of the sample were in the 1–20 µm and 2–40 µm size ranges, respectively. The grain size distribution histogram shown in Figure 5(b) also confirms this observation. This sample (1,700°C, 10 h) will be used for the data comparison from this point onward in the remainder of this paper, particularly because the 10 h sample had the larger average grain size than most other experiments conducted under similar conditions.

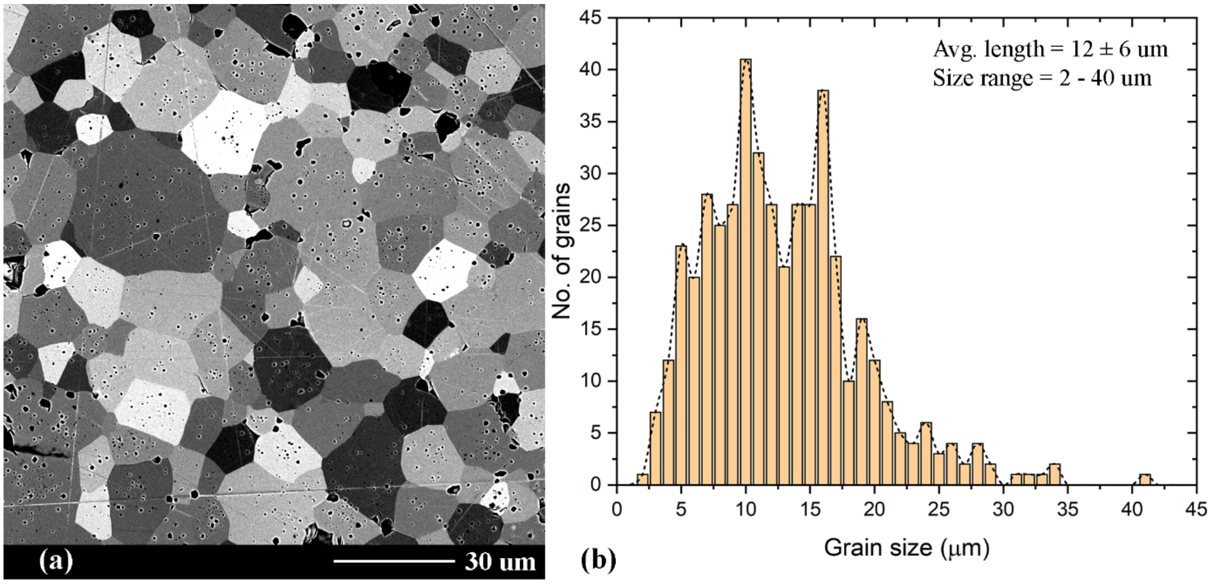

Figure 5. (a) An example BSE SEM micrograph and (b) the grain size distribution of undoped UO_2 sample after sintering.

To understand how the chromium dissolution and Cr_2O_3 dissociation temperatures affect the grain growth of Cr_2O_3-doped UO_2, three UO_2 samples doped using nominally 999 wppm Cr_2O_3 were fabricated using temperatures of 1,150, 1,465, and 1,655°C in an Ar-4%H_2 flowing gas environment. The maximum temperature of 1,655°C was used in the third sample to prevent any effects from the Cr-O liquid phase (an eutectic composition of $CrO_{(l)}$), which has been reported to form at ~1,665°C [17]. Both 1,465 and 1,655°C samples underwent the 1,150°C 10 h heat treatment, and the 1,655°C sample underwent the additional 1,465°C 10 h heat treatment, allowing the extra heat treatment steps for Cr solubilization in the UO_2 matrix before its dissociation. These three heat-treatments would therefore cover the evaluation of three conditions of chromium solubilization, Cr_2O_3 dissociation, and sample sintering. The sintered pellet densities of 1,150, 1,465, and 1,655°C samples were 10.40 (94.8% TD), 10.42 (95.1% TD), and 10.59 g/cm^3 (96.6% TD), respectively. As shown in Figure 66(a), the sample heated at 1,150°C only showed partial grain growth and a significant amount of porosity. The sample's 95% TD and the partial closure of the open porosity, as was observed in its microstructure, indicate that the Cr_2O_3 dissolution into the UO_2 structure has begun at this temperature. Both samples sintered at 1,465 [Figure 66(b)] and 1,655°C [Figure 66(c)] consisted of well-grown grains with low porosities, indicating close to full closure of pores compared with the 1,150°C sample. Figure 6(d) shows grain size distributions of these two samples; grain sizes of the samples sintered at 1,465 and 1,655°C ranged from 1–17 and 1–43 µm, with average grain size values of 5 and 12 µm, respectively.

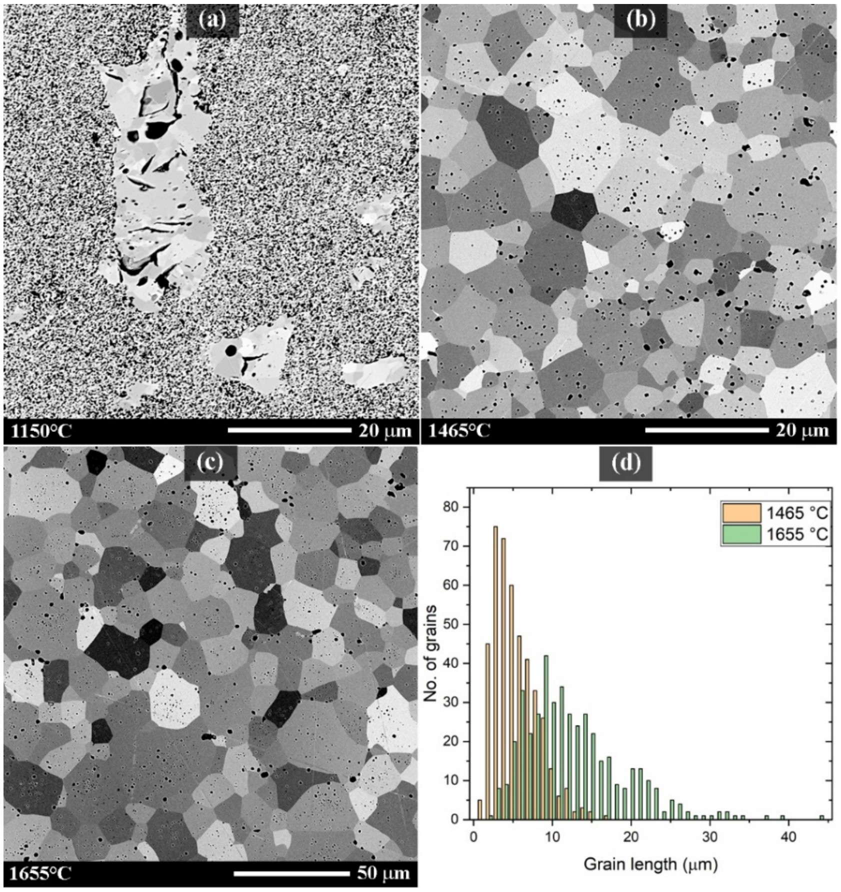

Figure 6. BSE SEM micrographs of the 999 wppm Cr-doped UO_2 samples heated at 1,150°C (a), 1,465°C (b), and 1,655°C (c) for 10 h. A histogram of the grain size distribution in the two samples heat treated at 1,465 and 1,655°C is shown in (d).

To determine the effect of sintering temperature on the UO_2 grain growth, a few more samples with 999–1,222 wppm Cr_2O_3 concentrations were fabricated using varied sintering temperatures. Figure 7 summarizes the data obtained for those samples. The sintered pellet densities were mostly ≥ 95% TD.

Overall, the average grain size of the nominally 1,000 wppm Cr_2O_3-doped UO_2 samples increased as the sintering temperature increased from 1,465 to 1,700°C. The smallest average grain size was 5 ± 3 µm at ≤1,500°C, whereas the largest average grain size was 19 ± 9 µm at 1,700°C. Samples sintered at 1,700 and 1,750°C did not show significant variation in their average grain sizes. Therefore, 1,700°C was used as the sintering temperature for most of the remaining samples.

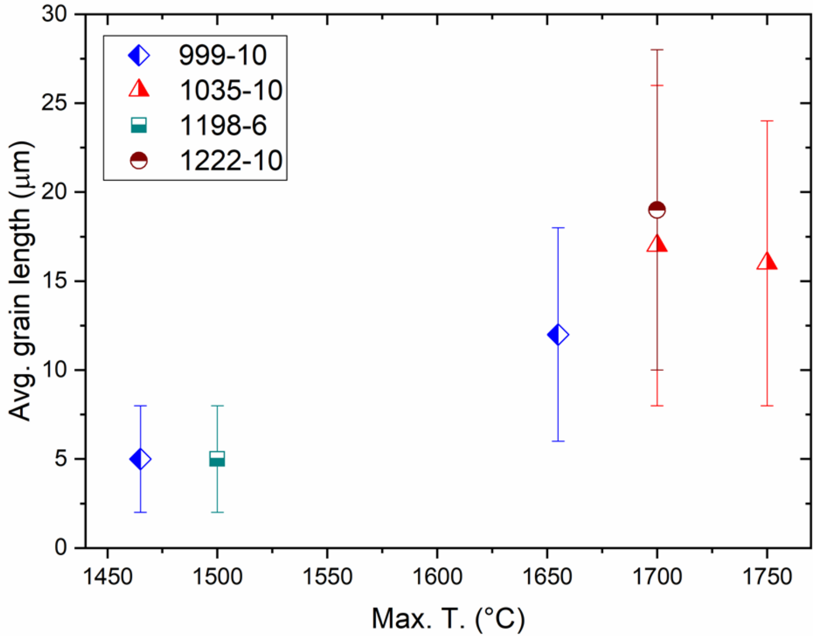

Figure 7. Average grain length of Cr-doped UO_2 samples as a function of sintering temperature. The legend indicates the varied nominal Cr concentrations and holding times of the samples at their sintering temperatures (e.g., 999-10 denotes 999 wppm Cr and 10 h holding time).

The overall change in the average grain size of the Cr-doped UO_2 samples sintered at 1,700 and 1,750°C with holding times up to 10 h is depicted in Figure 8(a). The average grain size of UO_2 increases with the increase in Cr concentration until it reaches a plateau with a value of 16–19 µm at ~1,000 wppm dopant concentration. As shown in Figure 8, the average grain size drops to 12–14 µm at >1,500 wppm Cr concentrations. The grain (number) density, shown in Figure 8(b), also decreased with the increase in Cr concentration up to ~1,000 wppm as a result of the grain size increase observed. As in the case of grain size variation, the grain density also goes up at >1,500 wppm Cr levels as expected due to the smaller grain sizes.

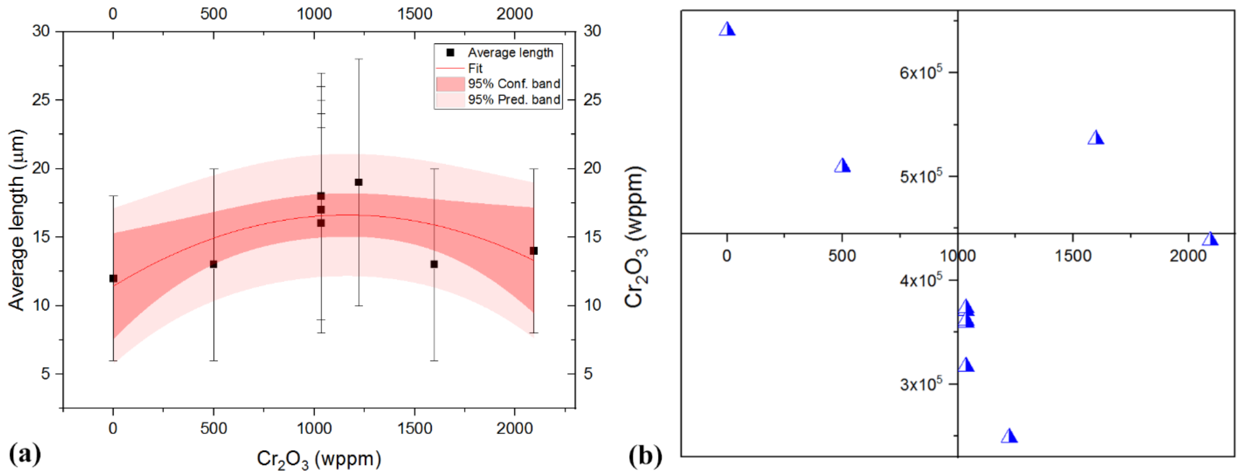

Figure 8. (a) The overall average grain size of the Cr-doped UO$_2$ samples as a function of Cr concentration. Samples sintered at 1,700 and 1,750°C using 6 and 10 h are plotted in this graph. (b) The change in the grain number density with respect to the Cr concentrations.

The grain size distribution of a few samples representing the varied average grain sizes determined is presented in Figure 9. The majority of the grains (~90%) of the undoped UO$_2$ sample can be observed in the 0–10 and 11–20 µm size ranging bins. A similar behavior is observed for the two samples with Cr$_2$O$_3$ concentrations >1,500 wppm. The UO$_2$ samples doped with ~1,000 wppm Cr$_2$O$_3$ consist of a considerable amount of large grains in the range of 21–61 µm.

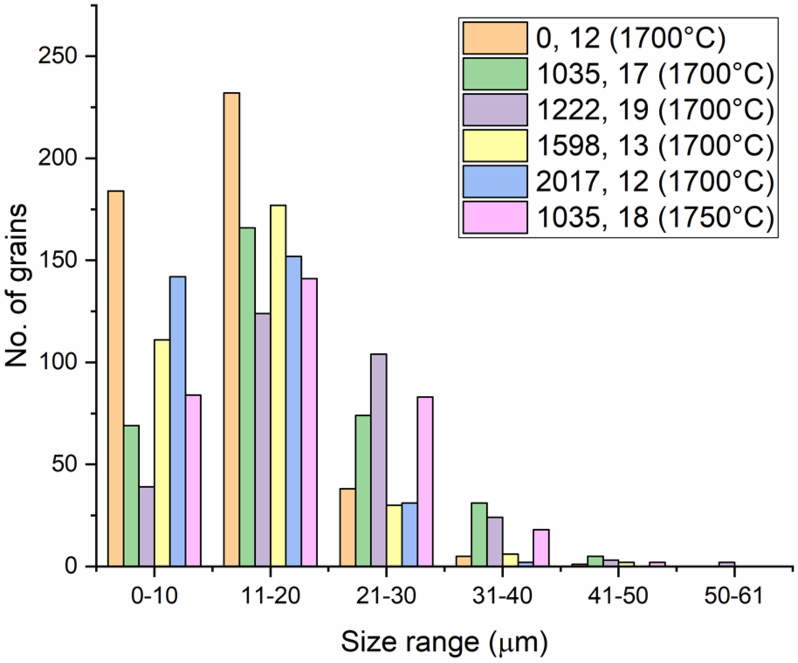

Figure 9. The grain size distribution of a few selected samples sintered at 1,700 and 1,750°C for 10 h. The first and second numbers in the legend represent the nominal Cr concentration in wppm and the average grain size in µm, respectively.

4. EXPERIMENTAL TEST METHODOLOGIES

Two methods were used for the data presented in this report. First, a biaxial flexure strength test was developed to be used for unirradiated UO_2. This method is standard in the community, but no systems presently in use at national laboratories, universities, or private companies were available to be used for irradiated materials. This report describes the operation and benchmarking of this system. Second, cantilever bend bar testing was previously developed and demonstrated by AFC for UO_2 [8–9]. This method has now been extended to provide preliminary data for Cr-doped UO_2 prepared as described above.

4.1 Biaxial Flexural Strength Tests

Common biaxial flexural strength tests include ring-on-ring, piston-on-3-balls, or the ball-on-ring, which all work to reduce friction during testing [18]. This study uses a ball-on-ring fixture as seen in Figure 10. The fixture consists of a base with a ring diameter of 13 mm, set screws to center the sample, a punch with an imbedded loading ball, and a punch alignment fixture. The imbedded loading ball is made of tungsten carbide, while the rest of the fixture is made of a high-strength CPM 10V tool steel.

The applied load was generated using an 810 series Materials Test System (MTS) mechanical test frame. The MTS TestSuite Software recorded the applied load and the displacement at a rate of 4 Hz. The generated force data are used to calculate transverse stress using Equations (1) and (2) above. The maximum calculated stress values were recorded as the TRS for each sample.

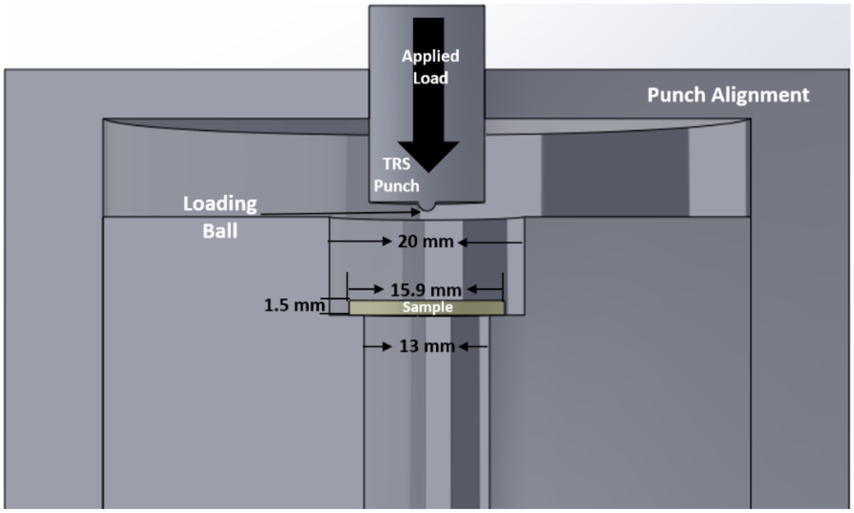

Figure 10. Cross-sectional schematic of TRS test fixture for right cylindrical samples.

4.2 Finite Element Analysis of Biaxial Flexure Tests

Numerical simulations were performed using the COMSOL Multiphysics software with an implicit static method. All interacting elements in this simulation were produced in COMSOL and chosen as deformable bodies. A two-dimensional axisymmetric model was generated by assuming a linear isotropic elasticity, described through Hooke's generalized law, and considering the geometrical axisymmetry of the test apparatus, material properties, and loading conditions. These simplifications enable a greater mesh control and higher accuracy while reducing computational costs and time. Figure 11 represents the geometry of the axisymmetric model used in this study. Table 2 summarizes the material properties of the test specimens and loading ball, also used in experimental calculations, used as parameters in the finite element (FE) model to evaluate the biaxial flexural strength fixture.

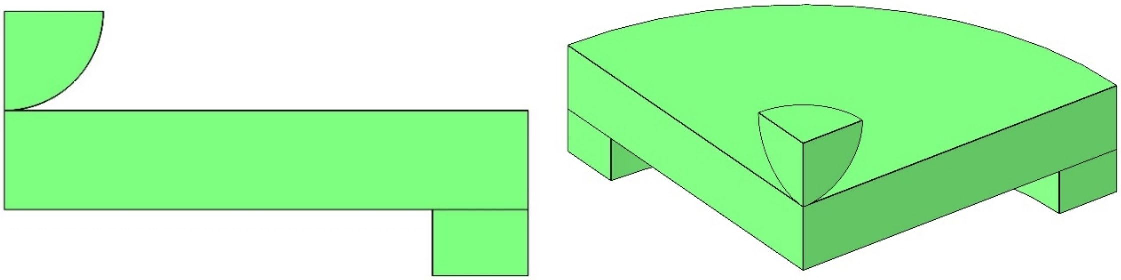

Figure 11. FE model geometry of the ball-on-ring test with the axisymmetric simplification.

Table 2. Material property parameters used in FE model.

Loading Ball [20]	**Material Properties**
The radius of the loading ball	1.5 mm
Density	15.7 g/cm^3
Elastic modulus	600 GPa
Poisson's ratio	0.22
Alumina [21]	
Density	3.92 g/cm^3
Elastic modulus	350 GPa
Poisson's ratio	0.22
YSZ [22-25]	
Density	6.02 g/cm^3
Elastic modulus	210 GPa
Poisson's ratio	0.23
MSZ [26]	
Density	5.72 g/cm^3
Elastic modulus	200 GPa
Poisson's ratio	0.23

Ceramic samples, supporting fixture, and the ball-loading sphere were considered as isotropic linear elastic materials defined by Hooke's generalized elasticity law. The contact between the loading ball, the sample, and the support ring was specified via a surface-to-surface discretization system considering frictionless conditions. This assumes a tangential response and a penalty method as a constraint enforcement method for the normal behavior. The support ring was fixed, while the loading ball was constrained to move only in the z-direction to elicit a response between the contacting elements of the ball-on-ring test. A rectangular mesh of 0.1 mm for the loading ball and support ring were used, while a mapped mesh of 0.04 mm was used for the sample, which yields 8,220 elements in total and 48,730 degrees of freedom solved for by the corresponding study step. Finally, the FE model used the experimental load at fracture, which is used in Equations (1) and (2) for determining TRS, to calculate the TRS for samples of each material.

4.3 Small-Scale Cantilever Beam Testing

The basics of the methodology used here have been described previously [8–9]. In brief, micromechanical test specimens were milled directly from the bulk UO_2 and doped UO_2 using a focused ion beam (FIB, FEI Scios). Mounting the samples on the testing stage prior to FIB milling ensures accurate alignment of the sample with the indenter. Microcantilever testing specimens were prepared with V-shaped notches that were precut at either a grain boundary or within the lattice. The exact dimensions varied between samples, but the general sample geometry was approximately 6–8 µm long, 2–3 µm tall, and 0.4–0.6 µm thick. Notches were prepared to have tip radii of curvature <50 nm since the measured fracture toughness would be approximately independent of notch radius in this range for the sample geometries tested [27]. The overall approach is similar to that described in more detail by Feng et al. [27]. Convergent beam electron diffraction patterns were obtained from all grains in each specimen at several tilt angles prior to mechanical testing. Because the testing platform is a single tilt stage, multiple tilts were used to locate the 0 tilt orientation in reciprocal space based on patterns simulated using the JEMS software. The orientation of each grain was determined manually based on these patterns. Mechanical tests were performed under displacement control at a rate of 1 nm s^{-1} during in situ imaging of the sample response.

5. RESULTS

The results presented here consist of benchmarking of the UO_2 ball-on-ring biaxial flexure fixture and presentation of small-scale cantilever beam testing results for Cr-doped UO_2. Future work will present TRS data for UO_2 and doped UO_2; this will represent a significant contribution to the literature and has not been previously reported. This will also allow analysis of the effect of dopants on fracture strength in unirradiated UO_2 using an established methodology. These data are important to allow for comparisons of fundamental fuel behavior in terms of how dopants and secondary phases affect mechanical properties. However, extension of this approach to irradiated fuels is not practical or likely possible. The large sample sizes needed for biaxial flexure strength measurement would be a challenge to irradiate and, even if possible, would suffer extreme temperature gradients, complicating interpretation of test results even if such a test could be performed in a hot cell. This shortcoming is where successful benchmarking of small-scale test methods may prove highly valuable. If trends observed in fracture testing of UO_2 using standard methods can be observed in small-scale testing, these same small-scale test methods can be used for irradiated fuel materials.

5.1 Biaxial Flexural Strength Test Method Validation

The TRS values found here, using the ball-on-ring biaxial flexure fixture, agree with those found in literature for MSZ and YSZ, as shown in Table 3. The lower end TRS values for alumina are about 36 MPa below the range found in the literature search performed. TRS values can span a large range depending on the density, microstructure, composition, sample preparation, and flaw size distribution. The characteristic strength for the alumina samples is within the TRS range reported in the literature, while the lowest recorded TRS value is slightly below this range. Figure 12 shows macro images of typical fractured samples for MSZ, alumina, and YSZ. Samples fractured into two to five pieces, with the majority (>75%) of samples breaking into three to four pieces. Figure 13 shows a representative stress vs displacement curve for alumina, MSZ, and YSZ.

Table 3. TRS values found in literature, determined in this study, and reported by vendor for the alumina, MSZ, and YSZ benchmark materials.

Material	TRS Reported in Literature (MPa)	Reference	TRS Determined in this Study (MPa)
Alumina	266–550	28–30	230–328
MSZ	400–900	31–34	611–893
YSZ	320–1240	35–38	595–936

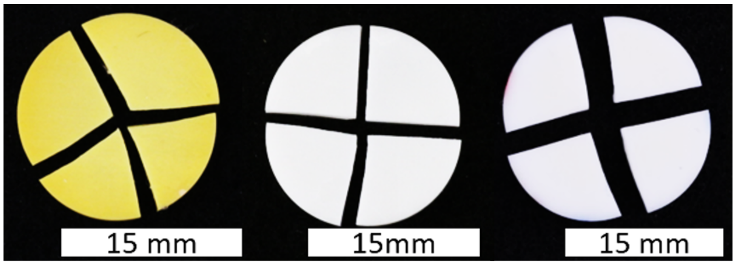

Figure 12. Benchmark samples post flexural strength tests from left to right are MSZ, alumina, and YSZ.

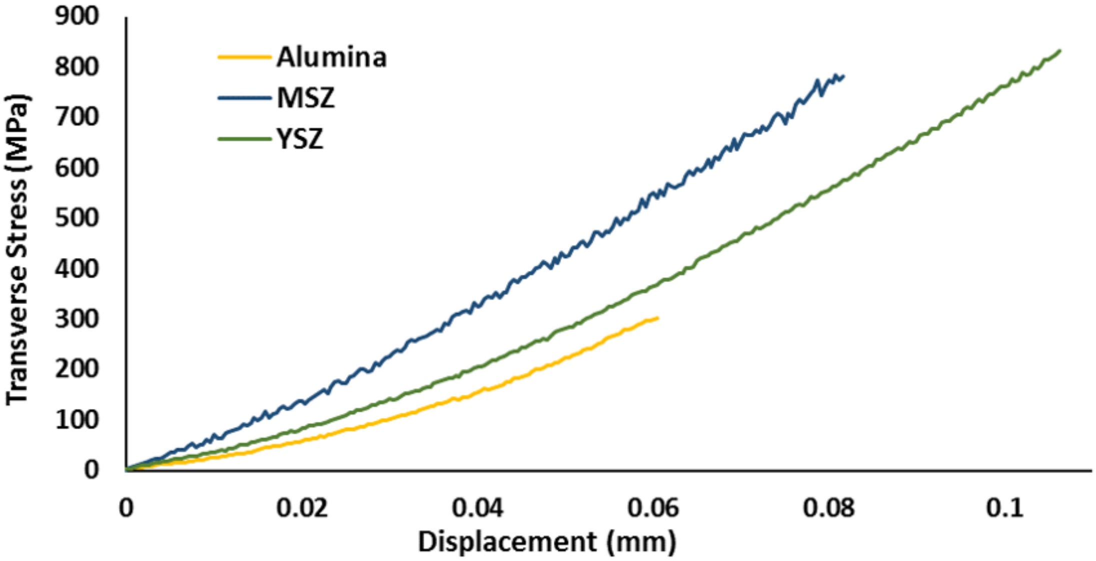

Figure 13. Representative stress vs displacement curves for each specimen type.

5.2 Fractography of Surrogate Materials

Figure 14 shows SEM images of the fracture surface for alumina, MSZ, and YSZ which can give some indication of the fracture mode for each sample type. The alumina samples have a trimodal microstructure which appears to impact the fracture mode. From the SEM image of alumina, it appears that the larger grains broke via a transgranular mode while the smaller grains fractured via an intergranular mode. Similar outcomes, mixed inter- and transgranular fractures, have been noted in the literature for alumina [28]. In the MSZ samples, transgranular failure was observed in the SEM images. High-magnification images of YSZ reveal an intergranular fracture mode.

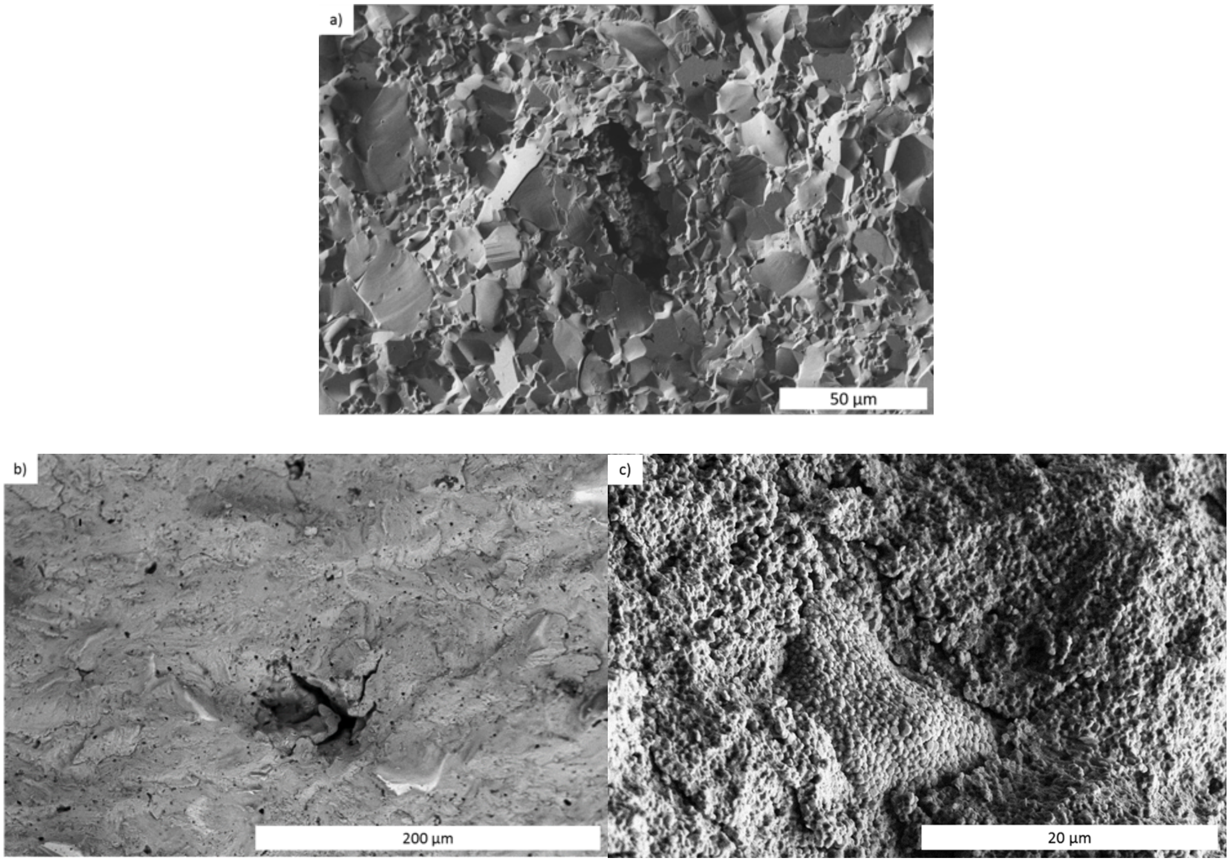

Figure 14. SEM fracture images of TRS tested benchmark samples from left to right are (a) alumina, (b) MSZ, and (c) YSZ.

5.3 Weibull Modulus of Surrogate Materials

Weibull statistics were used to evaluate the characteristic strength and reliability of all three ceramic specimen types. Weibull parameters were calculated using Equation (1) and a linear fit to the data (Figure 15), where the slope of the line is the Weibull modulus. In addition, the characteristic strength was extracted at the point when the probability of failure (P_f) is equal to 63.2%, as seen in Figure 16. Table 4 lists Weibull parameters and average TRS for each of the commercially available alumina, MSZ, and YSZ.

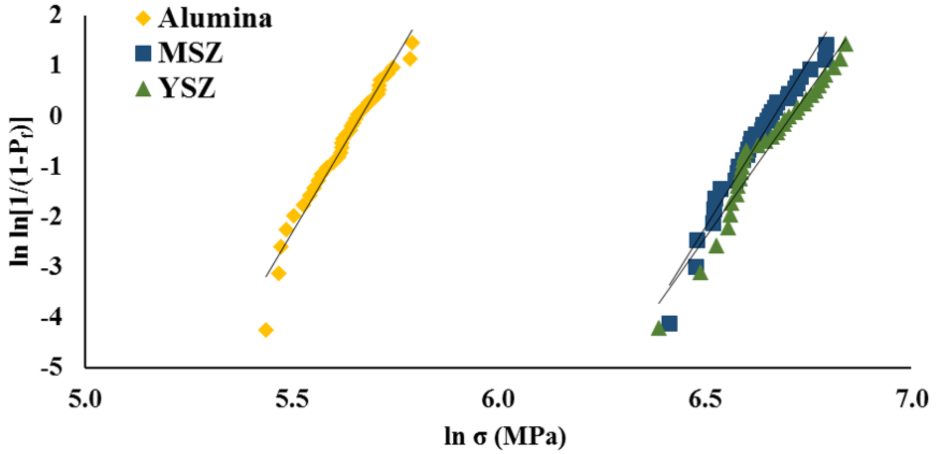

Figure 15. Weibull statistics plot was used to determine the Weibull modulus for alumina, MSZ, and YSZ, which were recorded as 13.8, 13.3, and 11.6, respectively.

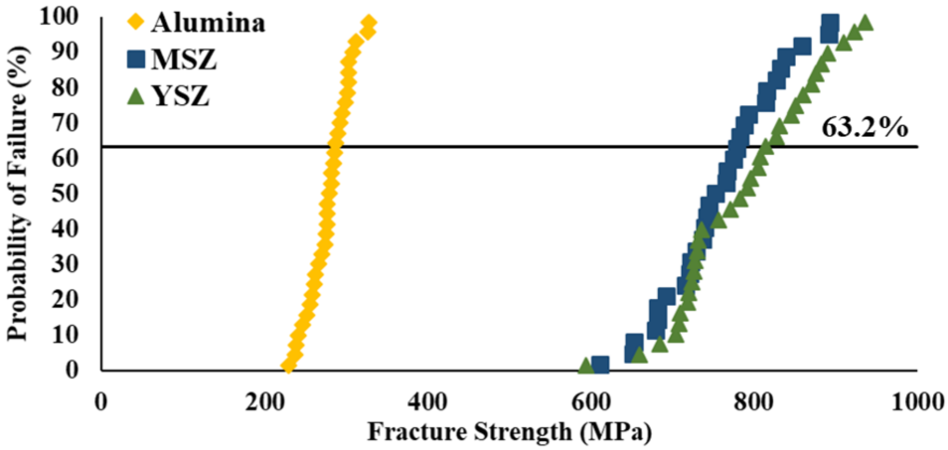

Figure 16. Probability of failure plot indicates the characteristic strength for alumina, MSZ, and YSZ at 286, 780, and 815 MPa, respectively.

Table 4. Weibull parameters for the alumina, MSZ, and YSZ benchmark samples.

Material	Average TRS (MPa)	Characteristic Strength [σ_0] (MPa)	Weibull Modulus [m]	Linear Fit [R^2]	No. Test Samples
Alumina	279	286	13.8	0.96	35
MSZ	757	780	13.3	0.96	33
YSZ	785	815	11.6	0.95	34

5.4 Finite Element Modeling Results

From experimental results for alumina, the average force registered at fracture was 340 N for a 1.50-mm sample, and this value was used to calculate the uniform pressure over the loading-ball top surface area. From the simulation, it was determined that the maximum tensile biaxial stress occurs on the bottom of the disk, as indicated by the red area in Figure 17, with a value of 290 MPa. The experimental TRS for this sample was measured as 293 MPa, which is in good agreement with the FE model results.

(a)

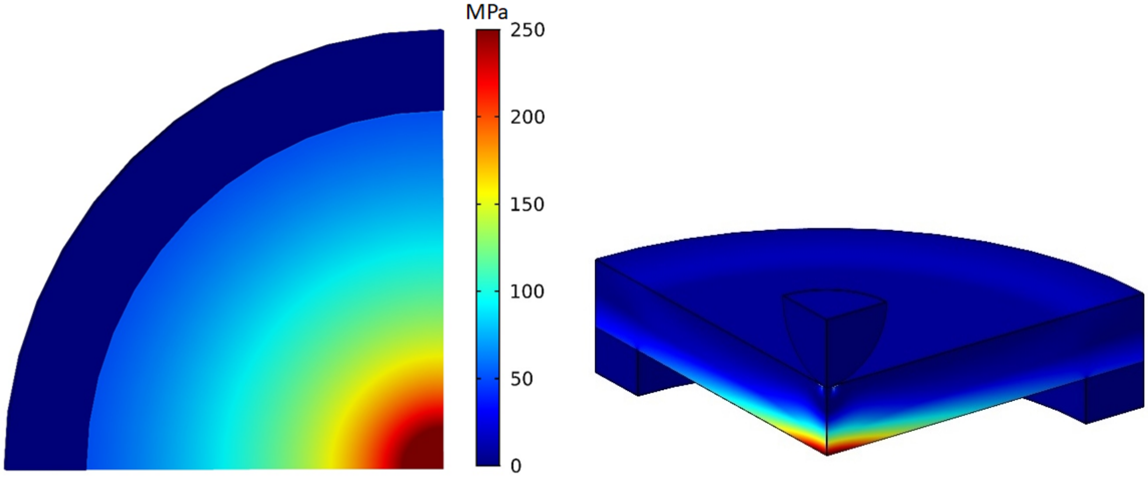

(b)

Figure 17. (a) mesh distribution and (b) maximum-principal stress distribution on the sample.

The predicted stress values at the tensile surface, along with the radial (σ_r) and tangential (σ_t) directions, are represented in Figure 18 and explain how these stresses change as a function of the radial length. σ_r and σ_t are equal at the center of the tensile surface of the disk. As the radial distance increases, the difference between these two stresses also increases. In addition, a sharp decrease in the stress pattern on the tensile surface of the specimen is clearly indicated in the plot produced by the FE model. This is due to compressive stresses where the sample makes contact along the supporting ring and indicates that it will not be a failure point in the ball-on-ring test [39].The FE analysis was conducted for alumina, YSZ, and MSZ, and the results are given in Table .

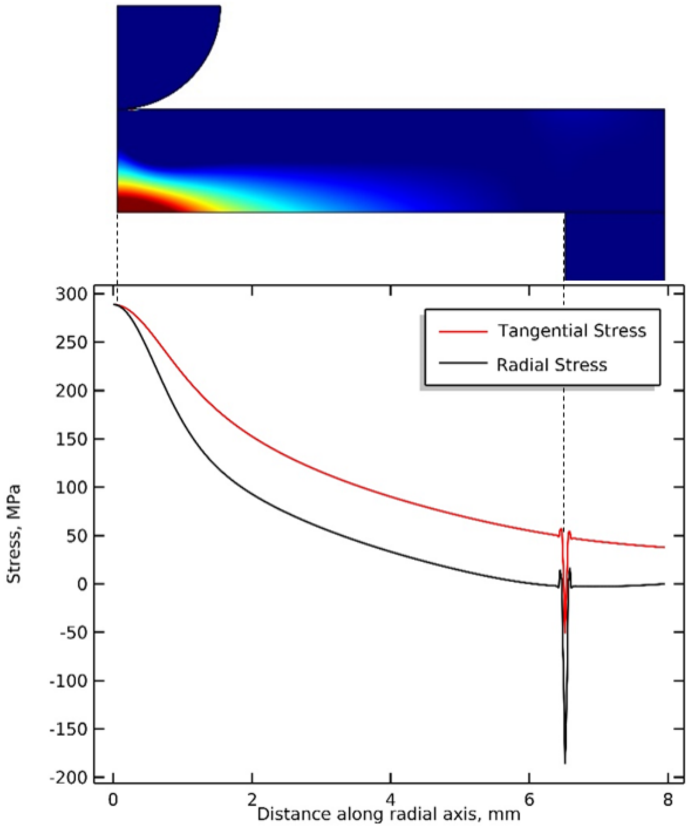

Figure 18. Tangential (σ_t) and radial (σ_r) stress distribution at the bottom tensile surface of the sample disk, shown in the upper portion of the figure.

Table 5. FE modeling results and corresponding TRS values for alumina, MSZ, and YSZ samples with varying sample thickness.

Material	**Thickness (mm)**	**Load at Fracture (N)**	**Corresponding Experimental TRS (MPa)**	**FE Model TRS (MPa)**
Alumina	1.50	340	293	289
	1.51	334	279	277
	1.48	309	267	279
YSZ	1.49	927	796	816
	1.51	1061	890	881
	1.49	1006	876	885
MSZ	1.51	995	839	824
	1.49	895	779	774
	1.50	1050	891	894

5.5 Benchmarking of TRS Data

Biaxial flexural strength tests performed on MSZ and YSZ resulted in TRS values within the range of those found in the literature. The values for TRS found in the literature spanned from 500-920 MPa for MSZ and YSZ. These large ranges in TRS values can be partly attributed to the fact that most studies do not report the concentration of Y_2O_3 or MgO in the zirconia samples, perform a microstructural analysis (i.e., grain size), indicate sample impurities, or discuss flaw size distributions. These factors can heavily impact the TRS of ceramic materials. For example, according to several numerical studies on the effects of phase transitions in zirconia where the transition leads to volume expansion, the material can undergo transformation toughening, which alters the sample strength [31, 32].

The TRS of the alumina samples was recorded as low as 36 MPa below the lower end of TRS found in the literature. The range of TRS values found in the literature for alumina was 280-290 MPa, which is a significantly smaller range than the stabilized zirconia samples. As previously mentioned, sample microstructure, density, impurities, flaw size distribution, and sample preparation can have a large impact on TRS. A majority of the TRS tests performed in the literature did not comment on many of these aspects, so it is difficult to make a direct comparison. The lowest TRS value recorded in this study was within less than 15% of the range for the alumina TRS values in the literature. The characteristic strength was within a 10% difference of the strength reported using Weibull statistics of 3-point bend bar tests of alumina published by L. Curkovic et. al [40]. In addition, the FE model also validated experimental results with its TRS calculation being within 5% of the experimental characteristic strength (Table). For the theoretical model to be validated, close agreement between experimental and numerical results are expected given that both methods used the experimental load at fracture to calculate TRS. Furthermore, microstructure, flaw size distributions, and other imperfections were not directly input into the FE model as it intrinsically considers those characteristics by using the experimental fracture load.

The Weibull statistics analysis provided Weibull parameters, such as the Weibull modulus and characteristic strength, which agree with TRS values found in the literature and Weibull modulus in the appropriate range for engineered ceramics (Table). The characteristic strengths were recorded as 286 MPa for alumina, 780 MPa for MSZ and 818 MPa for YSZ. The Weibull modulus, m, determines the reliability of the ceramic material, with a larger modulus indicting a more reliable material. A typical Weibull modulus for engineered ceramics, such as the materials tested in this work, typically range from 10 to 20 or higher (5). The Weibull moduli for alumina, MSZ, and YSZ were recorded as 13.8, 13.3, 11.6, respectively.

Fracture data exhibiting linear fit behavior indicate specimen types are good candidates for the Weibull distribution function. The data plotted in the Weibull plot showed the characteristic shape for the statistical model (Figure 15), with the required number of samples tested, which suggests this statistical model is an appropriate evaluation tool. Fracture data for the alumina, MSZ, and YSZ specimens had a linear fit with a coefficient of determination (R^2 value) of approximately 0.96, 0.96, and 0.95, respectively. For these samples, obtaining a Weibull modulus in the 10 to 20 range and obtaining a characteristic strength (σ_0) within the range found in literature are a good indication that the TRS test setup provides reliable data for these types of materials. FE modeling results also validated MSZ and YSZ characteristic strength results with an average of less than 8% difference (Table).

While the TRS and Weibull parameters found in this study are close to values published in the literature using other flexural strength test methods, it is important to acknowledge sources of error. Force values recorded for TRS calculations can be impacted by factors such as compliance in the test fixture and materials test frame. In addition, the sensitivity of the load cell, accuracy of density measurements, surface defects introduced during sample preparation, material property values used in calculations (i.e., Poisson's ratio), and precise sample thickness measurements can all impact the resulting TRS.

A significant concern in obtaining the flexural strength of ceramic materials is fracture points originating from edge defects. Common bulk material fracture points in ceramic samples occur at grain boundaries and other defects such as pores. In the limited number of samples examined, edge defect fractures were not observed but there is not enough evidence to make any claims on where the fractures originated. It was noted that alumina had a mixture of inter- and transgranular fractures, which is commonly noted in high-density alumina [28]. The mixture of inter- and transgranular fractures appears to coincide with the trimodal microstructure observed in the alumina samples. From the SEM image in Figure 14(a), it was noted that the larger grains appear to fracture transgranularly while the smallest grains fracture intergranularly. The MSZ samples appeared to have a transgranular fracture mode, while YSZ samples have an intergranular fracture mode, as shown in SEM images in Figure 14(b) and (c). Rice et al. [41] noted that intergranular fracture is dominant in fine-grained samples, and although this fracture mode is typically associated with lower strength samples, it is also associated with a fine microstructure which at lower temperatures which means higher strengths. The characteristic strengths for the MSZ and YSZ samples are in line with fracture surface images where YSZ resulted in a higher TRS.

5.6 Microcantilever Testing of UO_2 and Cr-Doped UO_2

Fracture testing of miniature cantilever beams has been presented previously as an attractive method to collect data on UO_2 both in the unirradiated and irradiated conditions [27]. Figure 19 provides an overview of the typical load-displacement curve and the cantilever testing as performed. The effects of dopant chemistry on lattice and grain boundary fracture toughness have also been measured in several doped UO_2 materials in order to survey several materials in which the dopant enhances grain growth. The results reported here focus on undoped UO_2, 1,035 wppm Cr-doped UO_2, 9500 wppm Cr-doped UO_2, and 1,035 wppm Cr and 108 wppm Al. The higher Cr content and Al-containing UO_2 samples were fabricated in the same manner as described in Section 3. The individual fracture toughness measurements are plotted in Figure 20(a) and (b) on a cumulative distribution plot. The mean lattice and grain boundary fracture toughness values and their standard deviations are plotted in Figure 20(c). In each case, the lattice exhibits marginally higher average fracture toughness than the grain boundaries. The distributions, however, significantly overlap, and the averages are within experimental error of one another. Each of the doped systems has lattice and grain boundary fracture toughness that exceed the undoped system, suggesting that the 3+ cation dopants used likely enhance the cohesive energy of the UO_2. The much larger 9500 wppm Cr did not, however, improve the fracture toughness relative to the 1,035 wppm Cr-doped material.

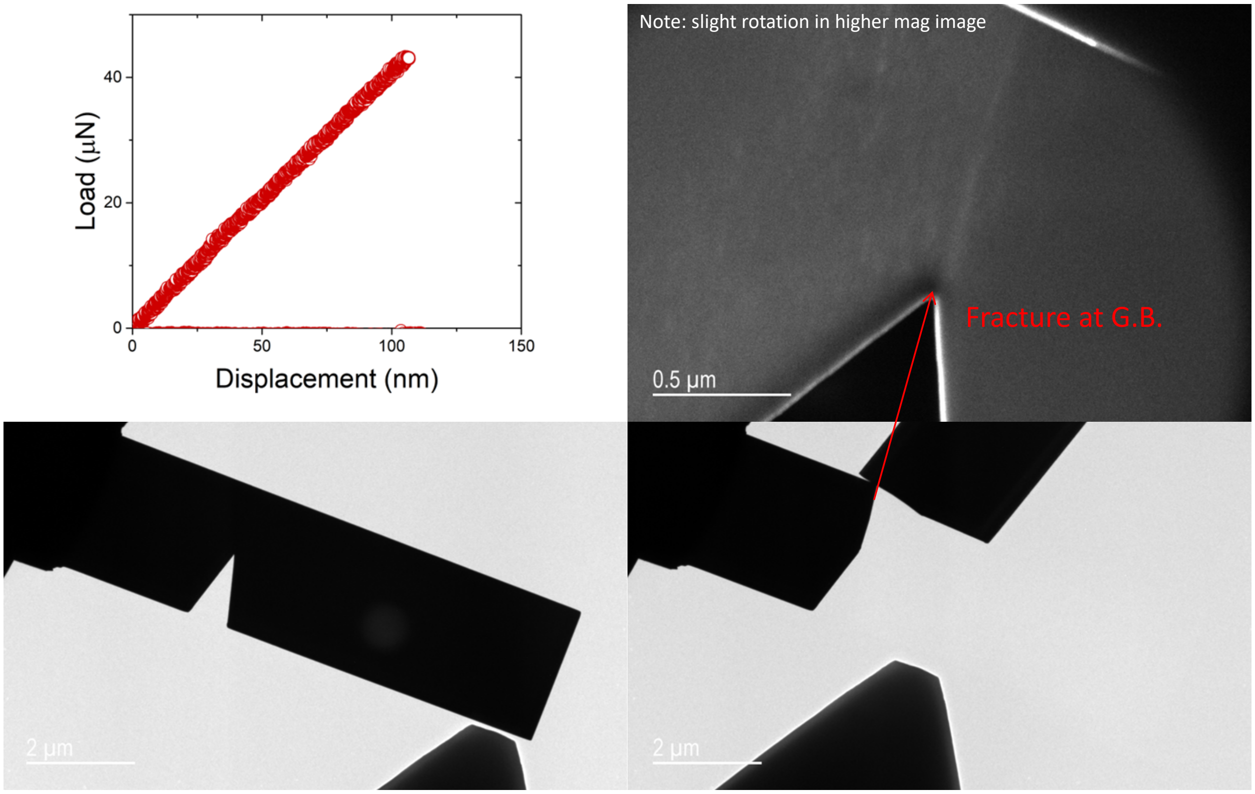

Figure 19. Microcantilever beam test of Cr-doped UO_2.

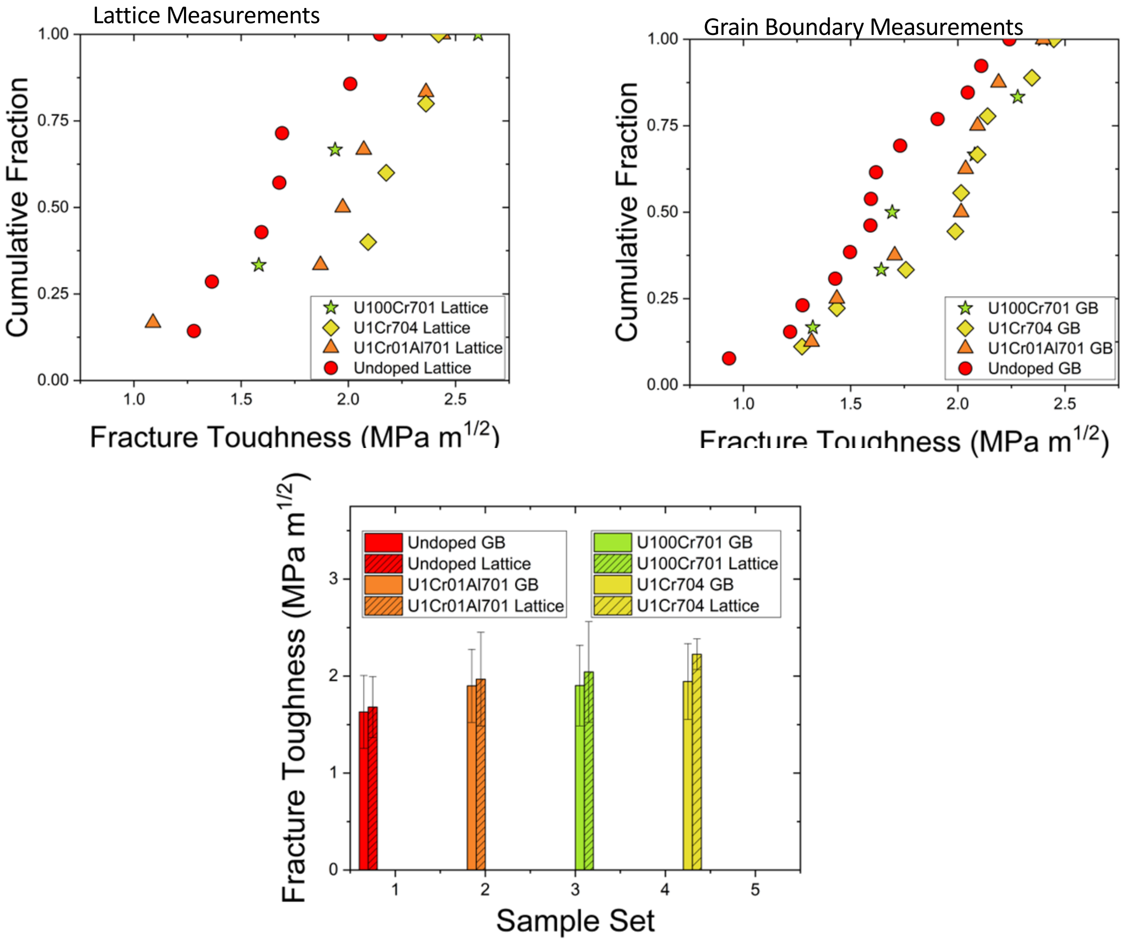

Figure 20. Cumulative plot of fracture toughness measured for pure UO_2 and Cr-doped UO_2 samples as determined both within the lattice and along grain boundaries. Here red circles indicated undoped UO_2, orange triangles are 1035 wppm Cr, green stars are 9500 wppm Cr, and yellow diamonds 1035 wppm Cr and 108 wppm Al.

Examination of the data plotted in Figure 19 reveals no statistically significant difference between all samples investigated. The similarity between lattice and grain boundary fracture toughness suggest that fracture should likely be transgranular or mixed mode. Example fracture surfaces are shown in Figure 21. In each case the fracture surfaces displace mixed mode fracture with a significant fraction of transgranular fracture.

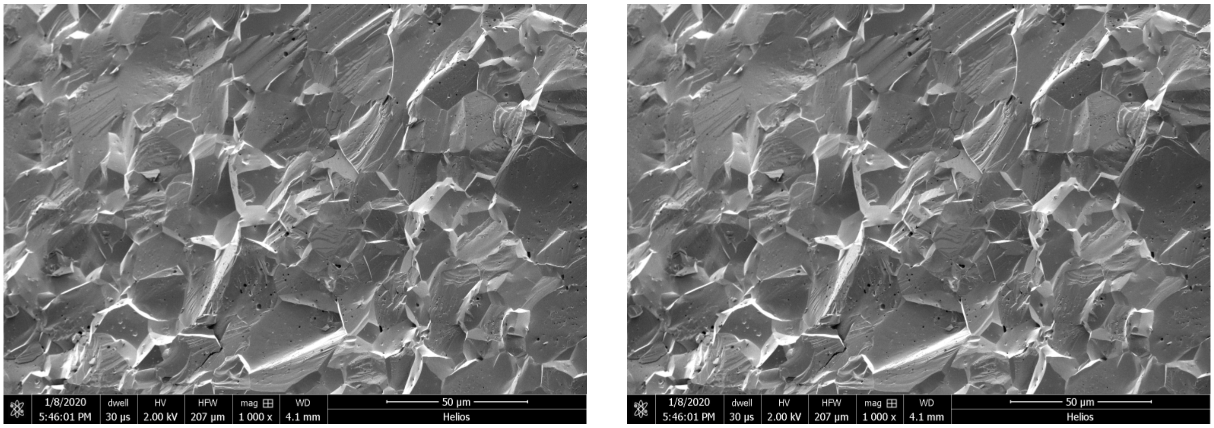

UO2702 **U1Cr704**

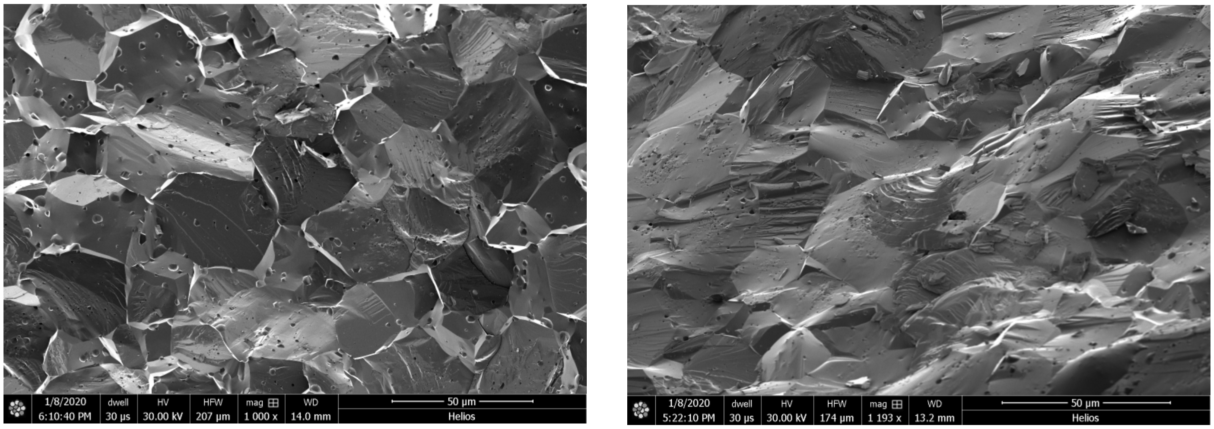

U100Cr701 **U1Cr01Al701**

Figure 21. Fracture surfaces of UO_2 samples tested as shown in Figure 20.

The outcomes observed here could be due to a number of possible factors. Foremost, detailed microscopic and chemical characterization of the samples has not been performed. The chemical and structural distributions of Cr are therefore not well understood and may impact the measurement. For example, Cr precipitation as Cr_2O_3 or other phases may result in minimal chemical differences in the doped UO_2 samples when tested at the length scale of microcantilever beam testing. The effects of Cr or other dopant additions on fracture behavior of UO_2 may also result in defect behavior that is simply unlikely to be captured by this technique or when testing <10 samples, as done here. Deployment of traditional techniques as benchmarked in this work will be highly informative for this purpose.

6. CONCLUSIONS

This report summarizes progress made in the characterization of fracture behavior in UO_2. It is recognized that the greatest potential for impactful experimental work in the area of mechanical properties of nuclear fuels is the expansion of small-scale mechanical testing methods to include validated cantilever beam testing. However, this method suffers from measurement of a relatively small sample volume that may not adequately capture the statistical nature of brittle fracture. Fracture toughness testing as determined using small-scale cantilever beam testing was extended to doped UO_2 in the present work, but no statistically significant effect of dopant was observed. This demonstrates the need to supplement and benchmark these techniques through the use of established methods such as biaxial flexure strength measurements. The deployment of such a method is demonstrated here and benchmarked for a range of standard ceramics. Future work will first develop TRS data for undoped UO_2 as a function of temperature and then extend testing to doped UO_2 as well as a range of relevant microstructures. An improved understanding of the fracture toughness of UO_2 will facilitate reexamination of small-scale methods against this dataset to build confidence for eventual application to irradiated fuels.

7. ACKNOWLEDGMENTS

The authors would like to acknowledge Alicia Raftery and Rachel Seibert for their review of the report and providing technical comments.

8. REFERENCES

[1] I.J. Hastings, A.D. Smith, P.J. Fehrenbach, and T.J. Carter, *Journal of Nuclear Materials*, **139**(2), 106–112 (1986).

[2] K. Une, K. Nogita, S. Kashibe, and M. Imamura, *Journal of Nuclear Materials*, **188**, 65–72 (1992).

[3] T. Zhang, R. Yue, X. Wang, and Z. Hao, *Nuclear Engineering and Design*, **330**, 463–479 (2018).

[4] Y. Sumi, L.M. Keer, and S. Nemat-Nasser, *Journal of Nuclear Materials*, **96**(1), 147–159 (1981).

[5] C. Bernaudat, *Nuclear Engineering and Design*, **156**(3), 373–381 (1995).

[6] J.M. Gatt, J. Sercombe, I. Aubrun, and J.C. Ménard, *Engineering Failure Analysis*, **47**, 299–311 (2015).

[7] Y. Zhang, P.C. Millett, M.R. Tonks, X.-M. Bai, and S.B. Biner, *Journal of Nuclear Materials*, **452**(1), 296–303 (2014).

[8] A. Nelson, S. Finkeldei, S. Dillon, B. Heuser, K. Terrani, *Development of small-scale mechanical property measurement methods for irradiated fuel samples,* ORNL/SPR-2019 (February 22, 2019).

[9] L. Feng, S. Finkeldei, B. Heuser, S. Dillon, and A. Nelson, “Grain boundary and lattice fracture toughness of UO_2 measured using small-scale mechanics,” *JOM,* **72**, 1–7 (2020).

[10] Y. R. Rashid, “Mathematical modeling and analysis of fuel rods,” *Nuclear Engineering and Design,* **29**(1), 22–32 (1974).

[11] M. C. Billone, R. O. Montgomery, Y. R. Rashid, and J. L. Head, “Advancements in the behavioral modeling of fuel elements and related structures,” *Nuclear Engineering and Design,* **134**(1), 23–36 (1992).

[12] B. Cox, “Pellet-clad interaction (PCI) failures of zirconium alloy fuel cladding — A review,” *Journal of Nuclear Materials,* **172**(3), 249–292 (1990).

[13] J. M. Gatt, J. Sercombe, I. Aubrun, and J. C. Ménard, “Experimental and numerical study of fracture mechanisms in UO_2 nuclear fuel,” *Engineering Failure Analysis,* **47**, 299–311 (2015).

[14] S. R.-D. C. D. Team, “SCDAP/RELAP5-3D Code Manual Volume 4: MATPRO - A Library of Materials Properties for Light-Water-Reactor Accident Analysis,” Idaho National Engineering and Environmental Laboratory (2003) 730.

[15] R. Sweet, A. Nelson, and B. Wirth, *Analysis of FeCrAl cladding and* UO_2 *fuel including discrete and smeared cracks, and fuel relocation*, Oak Ridge National Laboratory, ORNL/TM-2018/889, Oak Ridge, TN (2018) 38.

[16] A. G. Evans and R. W. Davidge, “The strength and fracture of stoichiometric polycrystalline UO_2,” *Journal of Nuclear Materials,* **33**(3), 249–260 (1969).

[17] A. Leenaers, L. de Tollenaere, Ch. Delafoy, S. Van den Berghe, "On the solubility of chromium sesquioxide in uranium dioxide fuel," J. *Nucl. Mater.* **317,** 62–68 (2003).

[18] S. Ban and K. J. Anusavice, "Influence of Test Method on Failure Stress of Brittle Dental Materials," *Journal of Dental Research,* **69**(12), 1791–9 (1990).

[19] A. Reckziegel, "Properties and Applications of High-Performance Ceramics Made of Zirconia," Aliaxis Utilities and Industry (2015).

[20] A. S. Savinykh, K. Mandel, S. V. Razorenov, and L. Kruger, "The Influence of the Cobalt Content on the Strength Properties of Tungsten Carbide Ceramics Under Dynamic Load," *Technical Physics*, **63**(3), 357–62 (2017).

[21] P. Auerkari, "Mechanical and Physical Properties of Engineering Alumina Ceramics," VTT Manufacturing Technology (1996).

[22] G. P. Cousland, X. Y. Cui, A. E. Smith, A. P. J. Stampfl, and C. M. Stampfl, "Mechanical Properties of Zirconia, Doped and Undoped Yttria-Stabilized Cubic Zirconia from First-Principles," *Journal of Physics and Chemistry of Solids*, **122**, 51–71 (2018).

[23] L. Łatka, D. Chicot, A. Cattini, L. Pawłowski, and A. Ambroziak, "Modeling of Elastic Modulus and Hardness Determination by Indentation of Porous Yttria Stabilized Zirconia Coatings," *Surface and Coatings Technology*, **220**,131–9 (2013).

[24] V. Menvie Bekale, G. Sattonnay, C. Legros, A. M. Huntz, S. Poissonnet, and L. Thomé, "Mechanical Properties of Cubic Zirconia Irradiated with Swift Heavy Ions," *Journal of Nuclear Materials,* **384**(1), 70–6 (2009).

[25] M. A. Borik, V. T. Bublik, A. V. Kulebyakin, E. E. Lomonova, F. O. Milovich, V. A. Myzina et al., "Phase Composition, Structure and Mechanical Properties of PSZ (partially stabilized zirconia) Crystals as a Function of Stabilizing Impurity Content," *Journal of Alloys and Compounds*, **586**, S231–S5 (2014).

[26] W-CJ. Wei and Y-P. Lin, "Mechanical and Thermal Shock Properties of Size Graded MgO–PSZ Refractory," *Journal of the European Ceramic Society*, **20**(8), 1159–67 (2000).

[27] L. Feng, R. Hao, J. Lambros, and S. J. Dillon, "The influence of dopants and complexion transitions on grain boundary fracture in alumina," *Acta Materialia,* **142**, 121–130 (2000).

[28] P. Auerkari, "Mechanical and Physical Properties of Engineering Alumina Ceramics," VTT Manufacturing Technology (1996).

[29] Y-M. Chen, R. J. Smales, KH-K Yip, and W-J. Sung, "Translucency and Biaxial Flexural Strength of Four Ceramic Core Materials," *Dental Materials*, **24**, 1506–11 (2008).

[30] J. Seidel, N. Claussen, and J. Rodel, "Reliability of Alumina Ceramics: Effect of Grain Size," *Journal of the European Ceramic Society*, **15**, 395–404 (1995).

[31] A. Reckziegel, "Properties and Applications of High-Performance Ceramics Made of Zirconia," Aliaxis Utilities and Industry (2015).

[32] Y. Kubota, M. Ashizuka, E. Ishida, and T. Mitamura, "Influence of Temperature on Elastic Modulus and Strength of MgO-Partially Stabilized Zirconia (Mg-PSZ)," *Journal of the Ceramic Society Japan*, **102**(8), 708–712 (1994).

[33] B. Kim, S. Jeon, C. J. V. Tyne, H. Park, and H. Lee, "Inter-Granular Phase Formation and Flexural Strength of MgO Partially Stabilized Zirconia by Al2O3 Additions," *Journal of Ceramic Processing Research*, **17**(5), 459–463 (2016).

[34] L. Jiang, S. Guo, Y. Bian, M. Zhang, and W. Ding, "Effect of Sintering Temperature on Mechanical Properties of Magnesia Partially Stabilized Zirconia Refractory," *Ceramics International*,42, 10593–10598 (2016).

[35] M. Cheng, W. Chen, and K. R. Sridhar, "Experimental Method for a Dynamic Biaxial Flexural Strength Test of Thin Ceramic Substrates," *Journal of American Ceramic Society*, **85**(5), 1203–1209 (2002).

[36] H. Yilmaz, C. Aydin, and B. E. Gul, "Flexural Strength and Fracture Toughness of Dental Core Ceramics," *The Journal of Prosthetic Dentistry*, **98**, 120–128 (2007).

[37] B. Stawarczyk, M. Ozcan, L. Hallmann, A. Enger, A. Mehl, and C. Hammerlet, "The Effect of Zirconia Sitnering Temperature on Flexural Strength, Grain Size, and Contrast Ratio," *Clin Oral Invest.,* **17**, 269-74 (2012).

[38] T. Kosmac, C. Oblak, P. Jevnikar, N. Funduk, and L. Marion, "The Effect of Surface Grinding and Sandblasting on Flexural Strength and Reliability of Y-TZP Zirconia," *Ceramic. Dent Mater.,* **15**(6), 426–33 (1999).

[39] G. D. Quinn, " NIST Recommended Practice Guide Fractography of Ceramics and Glasses," National Institute of Standards and Technology (2016).

[40] L. Curkovic, A. Bakic, J. Kodvanj, and T. Haramina, "Flexural Strength of Alumina Ceramics: Weibull Analysis," *Transaction of Famena* (2010).

[41] R. Rice, "Ceramic Fracture Mode-Intergranular vs Transgranular Fracture," United States: Alfred conference on fractography of glasses and ceramics (1996).